Research Article GU J Sci, Part A, 11(1): 24-40 (2024) 10.54287/gujsa.1407864

Gazi University
Journal of Science
PART A: ENGINEERING AND INNOVATION
http://dergipark.org.tr/gujsa

A New and Efficient Pan Sharpening Method Based on Optimized Pixel Coefficients

Tuba ÇAĞLIKANTAR[1] Melih Can KILIÇ[1*]

[1] *Gazi Universitesi, Fen Bilimleri Enstitüsü, Bilgisayar Mühendisliği Ana Bilim Dalı, Ankara, Türkiye*

Keywords

Pan Sharpening
Image Fusion
Remote Sensing
Optimization

Abstract

Pan sharpening aims to create a multispectral, high spatial resolution image by combining the multispectral image (MSI) with a high spatial resolution panchromatic image (PAN). Pan sharpening methods are performed between the MS image, which is the MSI image brought to PAN dimensions with the help of interpolation, and the PAN image. In this study, PAN sharpening is approached as an optimization problem. It is assumed that the optimal solution consists of multiplying the pixels of the MS image by optimized coefficients. It would be costly to optimize all the coefficients in this coefficient matrix one by one. For this reason, these coefficients were tried to be found with 5 different optimization-based methods. It was also compared with 19 different methods commonly used in the literature. 6 different evaluation criteria were used for this comparison. These comparisons were made on 3 different datasets. It has been observed that the proposed methods are superior to other methods.

Cite

Çağlıkantar, T., & Kılıç, M. C. (2024). A New and Efficient Pan Sharpening Method Based on Optimized Pixel Coefficients. *GU J Sci, Part A*, *11*(1), 24-40. doi:10.54287/gujsa.1407864

Author ID (ORCID Number)

0000-0001-5590-5307 Tuba ÇAĞLIKANTAR
0000-0002-6420-1456 Melih Can KILIÇ

Article Process

Submission Date 21.12.2023
Revision Date 08.01.2024
Accepted Date 17.01.2024
Published Date 30.01.2024

1. INTRODUCTION

An image from remote sensing has four basic resolutions. These four types of resolution are: temporal, radiometric, spectral, and spatial. The time difference between taking a remote sensing image of a location and taking another one after a predetermined amount of time is known as temporal resolution. The amount of bits used to indicate the electromagnetic energy acquired by remote sensing on a digital image is known as radiometric resolution. Pixel values in an image expressed with 8 bits take values between 0 and 255, whereas values in an image stated with 7 bits take values between 0 and 127. The wavelength range of the electromagnetic spectrum from which the image generated by remote sensing is obtained and the number of bands are related to spectral resolution. Narrower wavelength ranges correspond to higher spectral resolution for a given band. In other words, a band's sensitivity to, or the wavelength range it is received in, decreases with increasing spectral resolution. Spatial resolution can simply be defined as the area occupied by an image (pixel) on the surface. There is an inverse proportion between the amount of area a pixel represents on the ground and the spatial resolution.

Images are captured in various resolutions and across various electromagnetic spectrum bands by remote sensing systems. The MSI image has red, green, and blue bands from these sensors, which have a low spatial resolution yet provide a viewable image. Furthermore, PAN image with great spatial resolution is also acquired. When it comes to spatial resolution, the MSI which has color information is less precise than the PAN image. Fused high-resolution images with complementary data from multispectral bands are necessary for remote sensing applications such as feature extraction, classification, change detection, and clustering (Kurban, 2022). Pan sharpening is the term specifically used to describe image fusion techniques used to

*Corresponding Author, e-mail: mcan.kilic@os.gazi.edu.tr

produce an image with both color information and high spatial resolution. Interpolation is used to bring the MSI image to PAN image dimensions and the MS image is obtained.

The pan sharpening procedure is regarded as an optimization problem in this study. Every pixel in the MS image is multiplied by a coefficient to determine the ideal pan-sharpened image. Consequently, several approaches have been attempted to arrive at this optimal solution due to the large number of variables that require optimization. Low-pass PAN images were created by various methods to obtain an acceptable ratio between the PAN image and the low-pass PAN image. To our knowledge, this work is the third application of the Weighted Differential Evolution Algorithm (WDE) for pan sharpening in the literature (Civicioglu et al., 2020) WDE is applicable to several optimization-based pan sharpening techniques as a global minimizer. In addition, the study employed an objective function based on a Laplacian filter. The spatial information similarity between the low-pass PAN image and the MS image was compared using the Laplacian filter. The Laplacian filter regulates the transition between pixels by concentrating on the differences between image pixels and their spatial neighbors. This provides us with information on derivative, or border information, which is a crucial component of spatial information. The outcomes were contrasted with techniques from the literature that employed various evaluation standards. The amount of spatial features transferred from the PAN image and the amount of spectral features transferred from the MS image to the pan-sharpened image are measured using different metrics. The lack of a reference image to compare the final image to is one of the difficulties with pan sharpening. Some methods, like the Wald protocol (Wald et al., 1997), rely on the MSI image rather than the reference image to get over this problem.

Other than Component Substitution (CS) and Multiresolution Analysis (MRA) techniques, pan sharpening techniques have been studied and classified differently in the literature; however, more recent research has shown that these classifications are comparable. Amro et al. (2011) categorized pan sharpening techniques into five categories in their study: the CS family, the MRA family, the high frequency injection family, the relative spectral contribution family, and approaches based on image statistics. Vivone et al. (2020) looked at it in a more recent study and divided it into four categories: CS, MRA, VO, and machine learning (ML) techniques in 2021. Similar to Vivone, Meng et al. (2020) investigated it in 2021 within the following four headings: CS, MRA, VO, and deep learning (DL) techniques. Yilmaz et al. (2022) examined it under 6 headings: MRA, CS, Colour-Based (CB), DL, VO and hybrid methods. The basis of traditional CS approaches is to decompose the MS into components and replace the spatial context with PAN. Then, the PI image is obtained by inverse transformation. Matching the histogram of PAN and MS before component replacement will increase the correlation and create lower distortion (Ghassemian, 2016). Tu et al. (2001) expanded the traditional approach (Meng et al., 2019).

$$\mathrm{PI_i} = \mathrm{MS_i} - \mathrm{G_i} * (\mathrm{PAN} - \mathrm{I_L}) \quad (1)$$

PI is the fused image, G is the injection coefficient, $\mathrm{I_L}$ is the component that needs to be changed to PAN, and i is the representation of the bands. In general, CS approaches are simple to use and are successful in transferring spatial information. Many methods have been proposed in this regard. The focus of these methods is on accurate modeling of the relationship between MS and PAN (Vivone et al., 2020). However, they struggle to transfer the color information from the MS image. As examples of the most popular CS techniques, consider Brovey, Intensity Hue Saturation (IHS), Gram Schmidt (GS), Principal Component Analysis (PCA), Band Dependent Spatial Detail (BDSD).

In traditional MRA approaches, MS and PAN are moved to a different space with transformation functions. Spatial features from PAN are injected into the MS. Then the PI image is created by inverse transformation. The approach of traditional MRA techniques has been extended (Meng et al., 2019)

$$\mathrm{PI_i} = \mathrm{MS_i} - \mathrm{G_i} * (\mathrm{PAN} - \mathrm{PAN_L}) \quad (2)$$

PI is the fused image, G is the injection coefficient, $\mathrm{PAN_L}$ is the low-pass PAN, and i is the representation of the bands. Different MRA techniques have been tried to obtain G injection weight and $\mathrm{PAN_L}$ image (Meng et

al., 2019). Among the most well-known MRA methods, there are methods using wavelet transform like Discrete Wavelet Transform (DWT), à Trous Wavelet Transformation (ATWT). Numerous examples of generalized Laplacian pyramid (GLP) techniques have been given in the literature. These approaches rely on filters that utilize the Modulation Transfer Function (MTF) of the MS sensor by altering the injection coefficient estimate (Vivone et al., 2020). One such system that makes advantage of High Pass Modulation (HPM) is MTF-GLP-HPM (Vivone et al., 2020). While MRA-based techniques outperform CS-based techniques in terms of spectral feature preservation, they perform worse in terms of spatial feature preservation. However, according to Aiazzi et al. (2006), if the MTF approach is used, the performance will improve significantly. The paper is organized as follows: In the Introduction section, information about the pan sharpening process and the literature is given. In the second part, the method used in the paper is explained. In the third part, results and discussion are given. The fourth section contains the conclusion.

2. MATERIAL AND METHOD

Assuming that there is 1 most suitable pan sharpened image in the solution space for the pan sharpening process, this image is k times larger, with a separate coefficient for each pixel of the MS image.

$$\mathrm{PI_i} = \mathrm{MS_i} * \mathrm{MSK_i} \tag{3}$$

PI is the optimum solution in the solution space, MS is the multispectral image, and MSK is a coefficient matrix of MS dimensions. i represents the bands of the image. Finding the optimum value of each coefficient in this MSK matrix is an optimization problem. If we consider a 1024x1024 image, there will be a total of 3145728 coefficients that need to be optimized for 3 bands. Calculating the optimum value of these coefficients would be very costly. Therefore, calculating the coefficient matrix MSK in another way will reduce the computational cost.

$$\frac{\mathrm{PI}}{\mathrm{MS}} = \frac{\mathrm{PANHM}}{\mathrm{PANHM_{LP}}} \tag{4}$$

$$\mathrm{PI} = \mathrm{MS} * \frac{\mathrm{PANHM}}{\mathrm{PANHM_{LP}}} \tag{5}$$

PANHM is the histogram matching image of the PAN image with the MS, and $\mathrm{PANHM_{LP}}$ is the low pass version of the PANHM. The equality here shows that the ratio of the PI image to the MS image is also between PANHM and $\mathrm{PANHM_{LP}}$. Therefore, to ensure this equality and reach the PI solution, a suitable $\mathrm{PANHM_{LP}}$ must be created. For the purpose of pan sharpening, the PI is spatially similar to PANHM. Therefore, the $\mathrm{PANHM_{LP}}$ should likewise resemble the MS image spatially. The $\mathrm{PANHM_{LP}}$ picture was created in this study using five distinct techniques, or PL Methods.

2.1. PL Methods

PL Method-1 (PL1)

The $\mathrm{PANHM_{LP}}$ is created by multiplying each band with an appropriate coefficient after applying a Gaussian filter to the PANHM. Separate k coefficients for each band are calculated with the optimization algorithm. Bands are represented by i.

$$\mathrm{PANHM_{LP_i}} = \mathrm{Gauss}(\mathrm{PANHM_i}, 2) * \mathrm{k_i} \tag{6}$$

PL Method-2 (PL2)

The $\mathrm{PANHM_{LP}}$ is created by extracting the information that constitutes the spatial details from the PANHM. The MS is multiplied with the required coefficients after being subtracted from $\mathrm{MS_{LP}}$, the Gauss-filtered MS. Separate k coefficients for each band are calculated with the optimization algorithm. Bands are represented by i.

$$PANHM_{LP_i} = PANHM_i - \left(MS_i - MS_{LP_i}\right) * k_i \quad (7)$$

PL Method-3 (PL3)

In this method, it is assumed that the MS is a multiple of the PI image first reduced to X, Y dimensions and then re-extracted to its previous dimensions. Therefore, the same assumption is applied to the PANHM and tried to be verified. X, Y dimensions and k coefficients for each band are calculated with the optimization algorithm. H is height, W is width. These are the dimensions of PAN. Bands are represented by i.

$$PD_i = Interpolation(PANHM_i, size(X, Y)) \quad (8)$$

$$PANHM_{LP_i} = Interpolation(PD_i, size(H, W)) * k_i \quad (9)$$

PL Method-4 (PL4)

Discrete wavelet transform is applied to the PANHM (I_1) and MS (I_2) smoothed with a Gaussian filter. For the first component LL, an adaptive combination is performed with optimized k coefficients for all 3 bands, while the max method is used for the other components. Bands are represented by i. You can see the flow in Figure 1.

$$PANHM_{LP_i} = DWT\left(Gauss(PANHM_i, 2), MS_{LP_i}, k_i\right) \quad (10)$$

$$LL_i = (LL_{I_1} * k_i + LL_{I_2} * (1 - k_i)) \quad (11)$$

$$HH_i = \max\left(HH_{I_1}, HH_{I_2}\right) \quad (12)$$

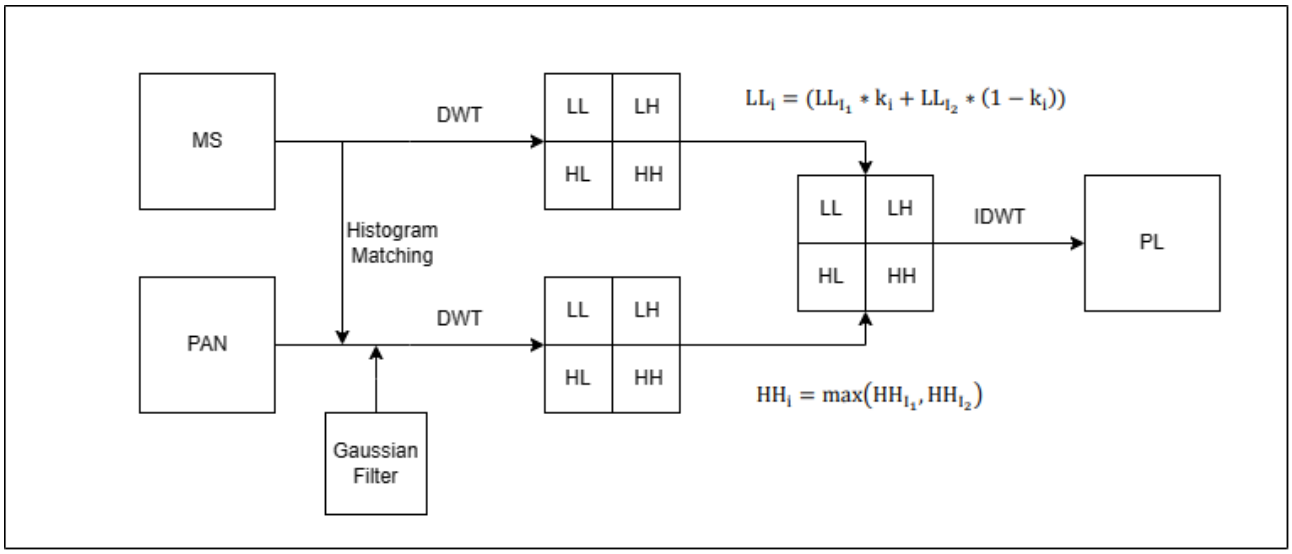

Figure 1. *Flow diagram of PL Method-4*

PL Method-5 (PL5)

PL is a modified version of PL Method-4. In this method, discrete wavelet transform is applied to the PANHM (I_1) softened with the Gaussian filter and the PL3 (I_2) created as in PL Method-3. H is height, W is width. These are the dimensions of PAN.

$$PANHMG_i = Gauss(PANHM_i, 2) \quad (13)$$

$$PD_i = Interpolation(PANHMG_i, size(\frac{H}{5}, \frac{W}{5})) \quad (14)$$

$$PL3_i = Interpolation(PD_i, size(PANHM_i)) \quad (15)$$

$$PANHM_{LP_i} = DWT(Gauss(PANHM_i, 2), PL3_i, k_i) \quad (16)$$

2.2. Optimization

WDE used as the optimization algorithm was developed by Civicioglu et al. (2020). WDE is a pattern matrix based Evolutionary Search algorithm (Civicioglu & Besdok, 2022) and also a stochastic, iterative and bi-population based algorithm. (Günen, 2021). Objective function (OF) consists of 2 parts. The first part is the SAM value calculated for MS and PI images. The second part uses the Laplacian filter to measure spatial information. This measurement is applied to MS (I_1) and $PANHM_{LP}$ (I_2) images, between which we want to have a high level of spatial similarity. After the Laplacian filter is applied to both images, the difference is calculated, and a 3-dimensional DIFF matrix enclosed in absolute value is obtained. With the help of Otsu thresholding, values below the limit in the DIFF matrix are eliminated. Finally, the average of all values is taken. H, W, C are the length, width, and number of bands of the MS image, respectively. (i = 1,2)

$$h = \text{Laplacian Filter} = \begin{bmatrix} 0 & 1 & 0 \\ 1 & -4 & 1 \\ 0 & 1 & 0 \end{bmatrix} \quad (17)$$

$$LAP_{I_i} = I_i \otimes h \quad (18)$$

$$DIFF_{ABS} = |LAP_{I_1} - LAP_{I_2}| \quad (19)$$

$$DIFF = DIFF_{ABS} * Otsu(DIFF_{ABS}) \quad (20)$$

$$OF_2 = \frac{1}{H * W * C} \sum_{h=1}^{H} \sum_{w=1}^{W} \sum_{c=1}^{C} DIFF_{h,w,c} \quad (21)$$

$$OF_1 = SAM(MS, PI) \quad (22)$$

$$OF = \frac{1}{2} (OF_1 + OF_2) \quad (23)$$

2.3. Evaluation Criteria

There are 2 approaches to evaluate pan-sharpened images, methods that need a reference image and methods that do not. The lack of a reference image needed in the first approach is a fundamental problem. Various approaches have been developed to overcome this problem. Wald et al. (1997) basically has two approaches. The first approach is based on the principle of reducing PI to MSI dimensions and making the two images similar to each other. The second approach is based on the similarity between the reference image obtained by the sensor in PAN dimensions and the PI. Since the mentioned image does not exist, the approach is implemented by reducing the dimension. After applying size reduction to the ratio between PAN and MSI, the original MSI is used as a reference. The QNR protocol was proposed by Alparone et al. (2008) in contrast to

techniques that call for references. As per Kallel (2014), high quality MS is not required for the QNR protocol to function. In this study, the first method in the Wald protocol was preferred in evaluation criteria requiring reference. This is because in the second method the quality of the reconstructed MSI image after down sampling is highly degraded. Since the dimensions of the images in the datasets are 1024x1024, the size of the reconstructed MSI image after subsampling is 64x64, which causes a large loss of information.

2.3.1. Evaluation criteria that require reference image

Spectral Angle Mapper (SAM)

SAM measures the angle between two spectral vectors. The operation is calculated for each pixel. The final value is calculated by averaging the values calculated for all pixels. If the value is close to zero, it means that the images are similar.

$$\mathrm{SAM}(x, y) = \arccos\left(\frac{\sum_{i=1}^{N} x_i y_i}{\sum_{i=1}^{N} x_i^2 \sum_{i=1}^{N} y_i^2}\right) \tag{24}$$

N indicates the number of bands. The pixels of the compared images are represented by x and y.

Root Mean Squared Error (RMSE)

RMSE calculates pixel level differences between images.

$$\mathrm{RMSE} = \sqrt{\frac{\sum_{x=1}^{H*W} \sum_{i=1}^{N} (X_i(x) - Y_i(x))^2}{H * W * N}} \tag{25}$$

The compared images are represented by X and Y. The pixels of the images are expressed as x, the length is H, the width is W, and the number of bands is N.

Erreur Relative Globale Adimensionnelle de Synthése (ERGAS)

ERGAS measures the quality of the resulting image by taking into account the normalized average error of each band. Increasing the value indicates distortion in the image, while decreasing indicates similarity to the reference image.

$$\mathrm{ERGAS} = 100 \frac{h}{l} \sqrt{\frac{1}{N} \sum_{i=1}^{N} \left(\frac{\mathrm{RMSE}(i)}{\mu(i)}\right)^2} \tag{26}$$

N refers to the number of bands. The average of the pixels of band i is denoted by μ(i). RMSE(i) means calculating RMSE only for band i. The dimensions of PAN and MS images are represented by h and l, with the ratio taken as 1/4 for Ikonos and QuickBird.

Universal Image Quality Index (UIQI - Q)

Q makes a measurement by taking into account the correlation, brightness and contrast between images. This measurement is divided into BxB parts of the image, calculated separately in each part, and averaged.

$$Q = \frac{4\sigma_{xy} \bar{x}\, \bar{y}}{\left(\sigma_x^2 + \sigma_y^2\right) + \left[(\bar{x})^2 + (\bar{y})^2\right]} \tag{27}$$

$$\bar{x} = \frac{1}{N} \sum_{i=1}^{N} x_i \tag{28}$$

$$\overline{y} = \frac{1}{N}\sum_{i=1}^{N} y_i \tag{29}$$

$$\sigma_x^2 = \frac{1}{N-1}\sum_{i=1}^{N} (x_i - \overline{x})^2 \tag{30}$$

$$\sigma_y^2 = \frac{1}{N-1}\sum_{i=1}^{N} (y_i - \overline{y})^2 \tag{31}$$

$$\sigma_{xy} = \frac{1}{N-1}\sum_{i=1}^{N} (x_i - \overline{x})\,(y_i - \overline{y}) \tag{32}$$

N is the total number of pixels in the image, while x and y denote individual image pixels. The Q value that was computed for each band was averaged for this study.

2.3.2. Evaluation criteria that do not require reference image

Quality With No Reference (QNR)

QNR consists of 2 separate metrics that examine images from a spectral (D_λ) and spatial (D_S) perspective.

$$QNR = (1 - D_\lambda)^\alpha (1 - D_S)^\beta \tag{33}$$

$$D_\lambda = \sqrt[p]{\frac{1}{N(N-1)}\sum_{i=1}^{N}\sum_{j=1,j\neq 1}^{N} |d_{i,j}(MS, PI)|^p} \tag{34}$$

$$D_S = \sqrt[q]{\frac{1}{N}\sum_{i=1}^{N} |Q(PI_i, PAN) - Q(MS_i, PAN_{LP})|^q} \tag{35}$$

$$d_{i,j}(MS, PI) = Q\left(MS_i, MS_j\right) - Q\left(PI_i, PI_j\right) \tag{36}$$

PAN_{LP} is the low pass version of the PAN image. N is the number of bands. In this study, $\alpha = \beta = p = q = 1$ was used.

2.4. Datasets and Compared Methods

The methods have been tested on 3 types of datasets: Pléiades (Vivone et al., 2014a; Open Remote Sensing, 2015), Ikonos (Shahdoosti & Ghassemian, 2014) and Rasat (Gezgin, 2013). In all datasets, the size of PAN images is 1024x1024 and the ratio between PAN and MSI is 4. The images are shown in Figure 2.

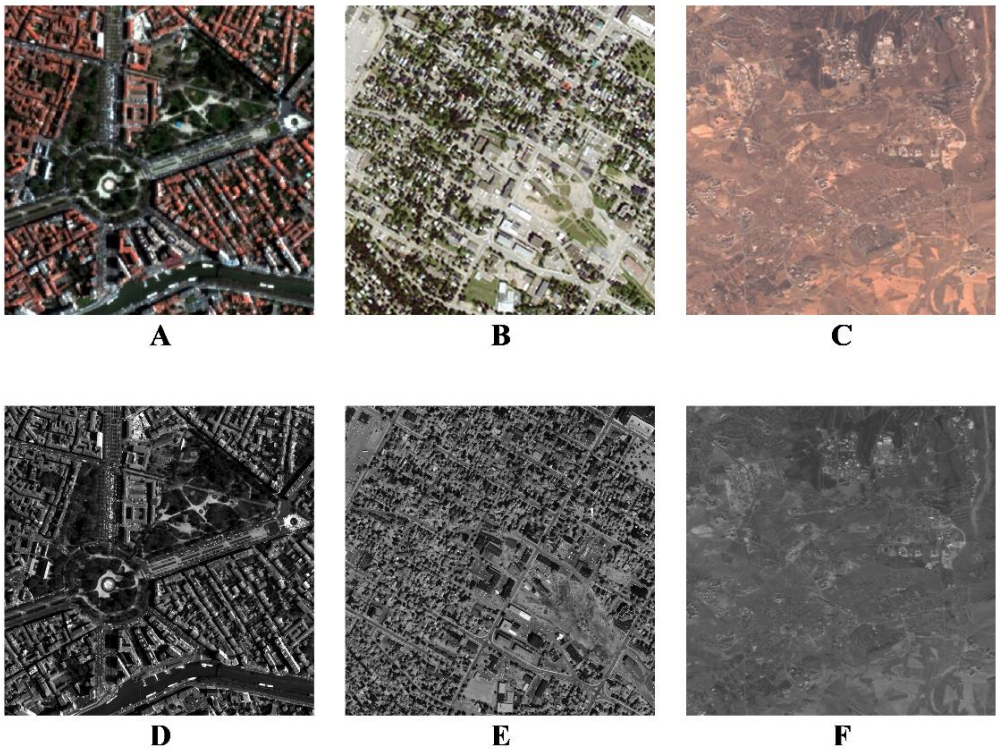

Figure 2. *Pléiades, Ikonos, Rasat dataset MS images A,B,C respectively, Pléiades, Ikonos, Rasat dataset PAN images D,E,F respectively*

The following methods, frequently used in the literature, were used for comparison:

CS methods: BT-H (Lolli et al., 2017), BDSD, C-BDSD (Garzelli, 2014), BDSD-PC (Vivone, 2019), GS, GSA.

MRA methods: AWLP (Otazu et al., 2005), MTF-GLP (MTF1) (Aiazzi et al., 2002; Aiazzi et al., 2006), MTF-GLP-FS (MTF2) (Vivone et al., 2018), MTF-GLP-HPM (MTF3) (Vivone et al., 2013), MTF-GLP-HPM-R (MTF4) (Vivone et al., 2017), MF (Restaino et al., 2016).

VO methods: FE-HPM (Vivone et al., 2014b), TV (Palsson et al., 2013), CSP (Civicioglu & Besdok, 2022).

DL methods: PNN (Masi et al., 2016), PNN-IDX (Masi et al., 2016), A-PNN (Scarpa et al., 2018), L-PNN (Ciotola et al., 2023).

3. RESULTS AND DISCUSSION

The evaluation results of the Pleiades, Ikonos, and Rasat data sets are shown in Tables 1, 2, and 3 of this section, respectively. Figures 3, 4, and 5 present the visual results in the same sequence. The results of evaluation criteria that require reference and those that do not require reference are located side by side. In the tables, CS, MRA, VO, DL and PL methods are listed one under the other and the winning values are marked in bold.

Table 1 shows that, except for some values for the Pleiades dataset, many methods produce similar results and the difference between them is small. In general, it seems that MRA, VO and PL methods produce results close to each other. CS methods are slightly behind them. It is seen that the PL3 method is superior to other methods in evaluation criteria that do not require reference. However, in those requiring reference, PL2 prevails in Q and ERGAS, and PL1 prevails in SAM. PL1 and PL2, although not spatially perfect, are more similar to the MSI image when subsampled according to the Wald protocol. This makes them stand out in evaluation criteria. Especially in PL2, directly benefiting from the MS image and using SAM in the objective function puts it

ahead in the SAM criterion. DWT-based PL4 and PL5 produced results close to other PL methods. There was not much difference for this dataset.

Table 1. *Pléiades dataset results*

Pléiades	D-λ	D-S	QNR	Q	SAM	ERGAS
BT-H	0.015086	0.10512	0.88138	0.8874	2.0684	8.9245
BDSD	0.015509	0.065875	0.91964	0.94454	2.2965	5.5375
C-BDSD	0.058699	0.029445	0.91358	0.91924	3.1281	6.4711
BDSD-PC	0.0068153	0.10579	0.88812	0.92477	2.7586	6.6378
GS	0.02214	0.1314	0.84937	0.85585	3.124	8.6249
GSA	0.035588	0.08787	0.87967	0.8931	8.6561	8.4995
AWLP	0.010393	0.046233	0.94385	0.97179	2.3634	4.0648
MTF1	0.030636	0.051806	0.91915	0.97058	2.1593	4.1855
MTF2	0.026306	0.051181	0.92386	0.97183	2.0306	4.0739
MTF3	0.13318	0.059385	0.81534	0.84878	5.982	994.5831
MTF4	0.013105	0.040637	0.94679	0.96619	2.0906	8.3344
MF	0.017977	0.067615	0.91562	0.95007	2.0175	5.4872
FE-HPM	0.022031	0.03094	0.94771	0.96249	2.0584	4.9903
TV	0.011811	0.059647	0.92925	0.9688	2.2762	4.2825
CSP	0.026358	0.063147	0.91216	0.91799	5.7096	6.5927
PNN	0.093615	0.083307	0.83088	0.85184	6.5904	8.5347
PNN-IDX	0.1213	0.1334	0.76148	0.62703	8.7662	14.878
A-PNN	0.064581	0.11914	0.82398	0.95796	4.4282	4.8877
L-PNN	0.031406	0.093676	0.87786	0.8971	3.9991	8.0688
PL1	0.012639	0.040972	0.94691	0.80247	1.9318	11.4409
PL2	0.027111	0.22301	0.75592	0.9764	2.0628	3.7289
PL3	0.0059155	0.008558	0.98558	0.95968	1.9445	4.7549
PL4	0.018083	0.062969	0.92009	0.95693	2.1216	4.9929
PL5	0.014618	0.045644	0.94041	0.96185	1.9566	4.7159

In the visual results of the Pleiades dataset, in Figure 3, it is seen that DWT-based PL methods can carry both spectral and spatial information in a balanced manner. In this dataset, MTF-based methods injected spatial information well. VO methods appear to convey spectral information well. CS methods could not transfer spatial and spectral information in a balanced manner.

In Table 2, the average of all QNR values is 0.7695 and the variance is 0.0177. The mean of the Pleiades dataset is 0.8824 and the variance is 0.0064. These values tell us that the Ikonos dataset is more discriminative in comparing the methods. D-λ values in the Ikonos dataset are similar to those in the Pleiades dataset. Although the variance is almost the same between D-S values, there is a difference of 0.11 on average. This shows us that this dataset is more difficult in terms of carrying spatial information.

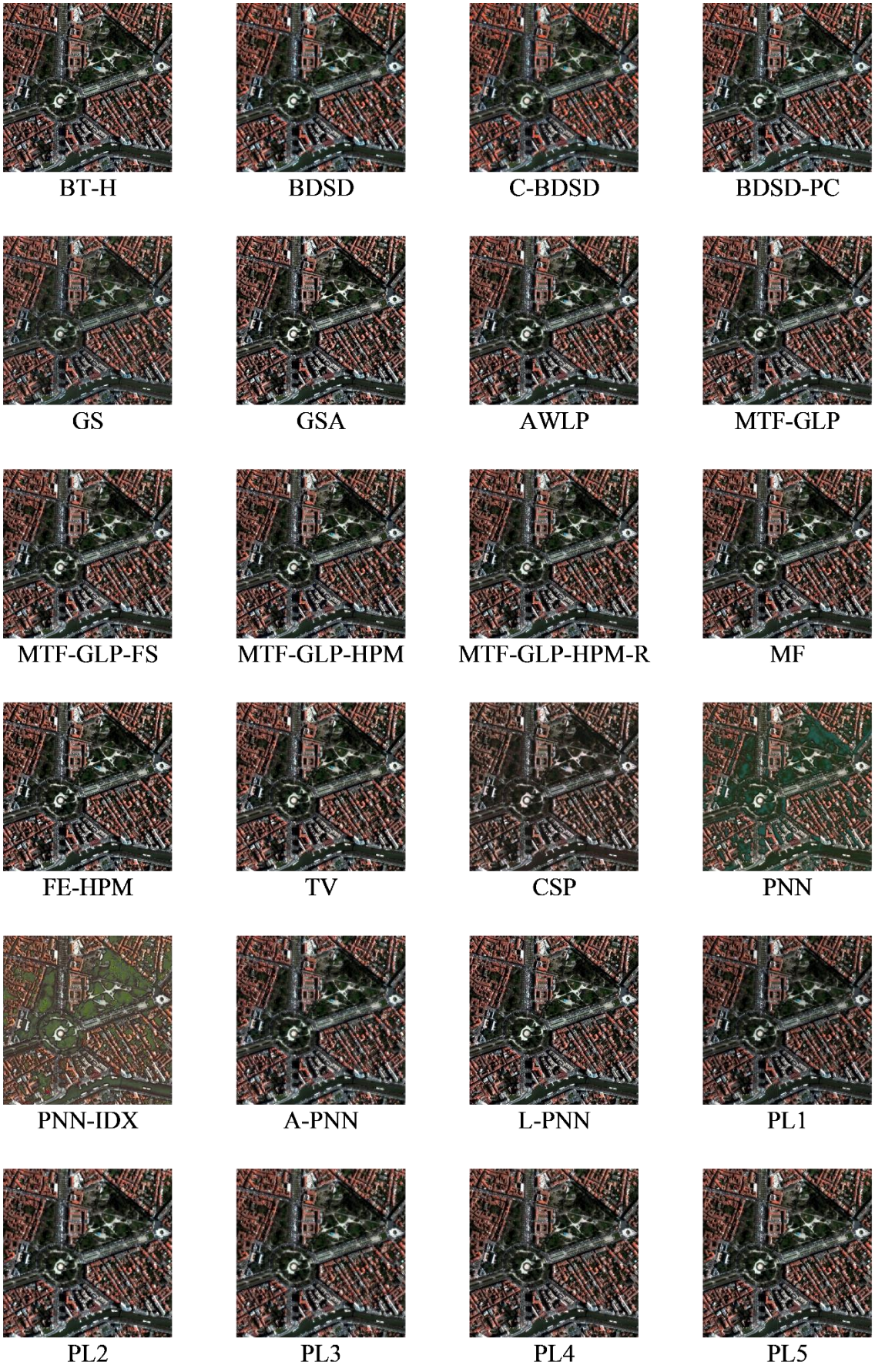

Figure 3. *Pléiades dataset results*

Table 2. *Ikonos dataset results*

Ikonos	D-λ	D-S	QNR	Q	SAM	ERGAS
BT-H	0.050228	0.14701	0.81015	0.29874	8.8132	49.3399
BDSD	0.022886	0.11062	0.86903	0.98079	0.86477	1.8819
C-BDSD	0.041303	0.080003	0.882	0.97971	1.5667	1.9298
BDSD-PC	0.012479	0.12237	0.86667	0.98381	0.70801	1.7972
GS	0.027725	0.45209	0.53272	0.44585	2.6587	10.2561
GSA	0.017065	0.24919	0.73799	0.87853	1.6225	5.1437
AWLP	0.018906	0.202	0.78291	0.98106	0.55645	1.9158
MTF1	0.032489	0.20205	0.77202	0.97438	1.0674	2.2848
MTF2	0.011005	0.17164	0.81924	0.99332	0.39928	1.1147
MTF3	0.2051	0.088696	0.72439	0.73453	5.2431	61.2218
MTF4	0.0097461	0.14872	0.84299	0.99312	0.24207	1.1311
MF	0.023117	0.18625	0.79494	0.96684	0.81553	2.6188
FE-HPM	0.021544	0.16457	0.81743	0.98384	0.56367	1.8028
TV	0.029596	0.19318	0.78295	0.9607	2.7201	3.0736
CSP	0.016969	0.29922	0.68889	0.89976	2.1917	4.3224
PNN	0.04607	0.18722	0.77533	0.95502	4.589	3.0803
PNN-IDX	0.056905	0.21731	0.73815	0.88718	4.3976	4.7213
A-PNN	0.067098	0.085699	0.85295	0.98693	2.5538	1.5769
L-PNN	0.021057	0.16792	0.81456	0.99061	12.944	13.335
PL1	0.014623	0.15275	0.83486	0.8674	1.2313	11.0606
PL2	0.012346	0.071896	0.91665	0.99657	0.39531	0.81308
PL3	0.018227	0.17256	0.81236	0.94033	1.064	3.4762
PL4	0.023405	0.36667	0.61851	0.83664	1.8075	5.5437
PL5	0.017267	0.18205	0.80382	0.97969	0.58728	2.0151

When we examine Figure 4, it can be seen that CS methods are not very successful in transferring spectral information in this data set. In the measurements, it is seen that PL2 is superior in 4 out of 6 measurements. There is also a big difference in results between other PL methods. When we examine the image, it can be seen that it conveys the spectral information in the MS image very well. MTF4 was successful in conveying spectral quality by obtaining the best values in two criteria that were successful in measuring spectral features.

When the Rasat dataset in Table 3 results are examined, the results of many methods are very close to each other, especially in methods that require reference. We can attribute this to the fact that the spatial resolution of Rasat data is not as high as other datasets. It is seen that CS methods are generally superior to MRA methods. However, there are no major differences.

When we examine the images in Figure 5, it is seen that the brightness value of the PL1 image cannot be adjusted well. The PL1 method fell far behind other PL methods in D-S, QNR and ERGAS criteria. The reason for this may be that the image is created with the help of only 3 optimized coefficients in total, 1 per band.

It has been observed that PL methods are superior to other methods frequently used in the literature in many evaluation criteria. Although there is no superior visual spatial performance, especially in evaluation criteria that require reference, it is seen that spectral information is conveyed well. However, it has been observed that visual evaluation and objective evaluation criteria do not always yield the same results. Civicioglu and Besdok (2024) mentioned, color distortion was observed in CS methods, especially in the Ikonos data results. Aiazzi et al. (2006) mentioned, it was also seen in this study that MRA methods using the MTF approach are successful in transferring spatial information. Feng et al. (2024) also mentioned, it has been observed that MRA-based approaches generally provide superior spectral preservation results than CS-based methods.

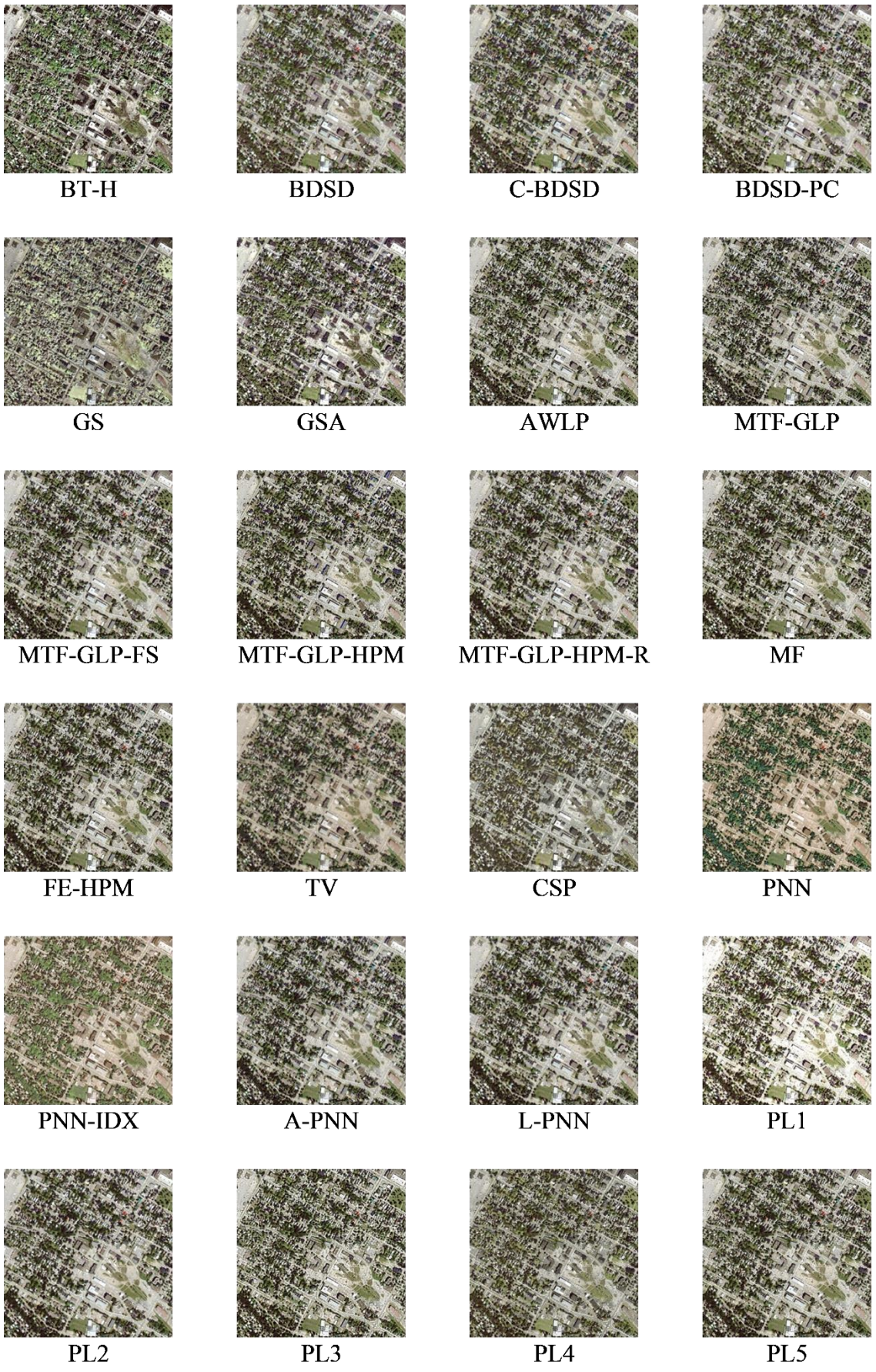

Figure 4. *Ikonos dataset results*

Table 3. *Rasat dataset results*

Rasat	D-λ	D-S	QNR	Q	SAM	ERGAS
BT-H	0.037075	0.071621	0.89396	0.91528	0.68672	1.1669
BDSD	0.0034129	0.061771	0.93503	0.91312	0.5211	1.0995
C-BDSD	0.0082902	0.058071	0.93412	0.91348	0.53358	1.0705
BDSD-PC	0.0062483	0.074998	0.91922	0.91039	0.52178	1.0977
GS	0.0059761	0.099265	0.89535	0.9022	0.51035	1.11
GSA	0.011029	0.068409	0.92132	0.91389	0.52601	1.1432
AWLP	0.0066989	0.042147	0.95144	0.89771	0.53709	1.2053
MTF1	0.021725	0.037048	0.94203	0.89747	0.52678	1.2141
MTF2	0.019214	0.040237	0.94132	0.89738	0.52917	1.216
MTF3	0.022773	0.037616	0.94047	0.89754	0.52396	1.2194
MTF4	0.017167	0.036352	0.94711	0.89797	0.52621	1.2135
MF	0.026001	0.040301	0.93475	0.87225	0.55609	1.3807
FE-HPM	0.018626	0.025861	0.95599	0.88207	0.53672	1.2749
TV	0.022874	0.045822	0.93235	0.96262	1.5805	1.6298
CSP	0.022217	0.092562	0.88728	0.89324	0.78026	1.1809
PNN	0.052711	0.053492	0.89662	0.90627	1.7789	1.4354
PNN-IDX	0.10696	0.052078	0.84653	0.89197	2.9251	1.8026
A-PNN	0.047995	0.15749	0.80207	0.89221	0.99395	1.2328
L-PNN	0.055579	0.065375	0.88268	0.9131	0.64214	11.063
PL1	0.0065028	0.15521	0.8393	0.75687	0.52235	8.4083
PL2	0.0073171	0.010126	0.98263	0.89479	0.52277	1.1925
PL3	0.0066768	0.045148	0.94848	0.89463	0.5203	1.184
PL4	0.029312	0.05911	0.91331	0.90036	0.54958	1.1657
PL5	0.012472	0.024136	0.96369	0.89831	0.52181	1.1904

4. CONCLUSION

In this study, pan sharpening is approached as an optimization problem. The optimum solution was tried to be achieved by optimizing the pixels of the MS image. 5 different optimization-based methods have been tried. The purpose of these methods is to create a low-pass PAN image. The ratio between low-pass PAN and PAN was used to obtain the PI image. WDE algorithm was used as the optimization algorithm. Laplacian filter and SAM were used as objective functions. The proposed methods have been proven to be superior to other methods in many criteria. When we compared the proposed methods among themselves, it was seen that DWT-based PL methods were left behind compared to other PL methods. This may be due to not providing the correct combination. It was observed that the band-based coefficient method used in the methods was insufficient. Creating a compositing factor of 1 for the entire band sometimes caused the image not to be produced at the desired quality. To overcome this shortcoming, the MS image can be divided into segments and a coefficient can be optimized for each segment in each band. Thus, region-based merging can produce a higher quality image. Additionally, in the PL1 method, there appears to be a brightness issue. To solve this problem, the PL1 method can be transformed into an optimization-based contrast stretching method. It has been observed that the ratio between PAN and low-pass PAN will bring us closer to the optimum solution. Optimization-based solutions used to create the low-pass PAN have been shown to be useful.

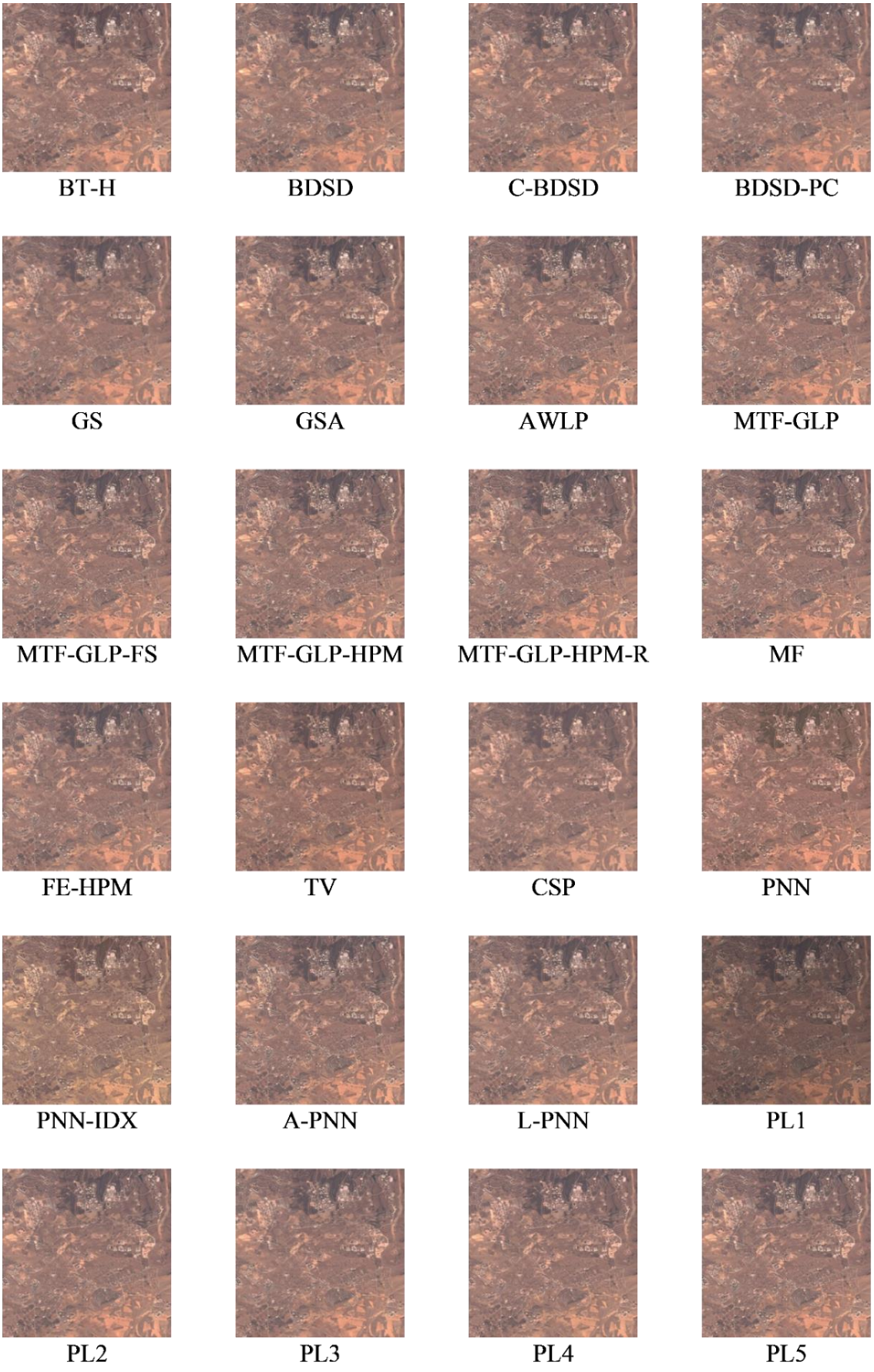

Figure 5. *Rasat dataset results*

ACKNOWLEDGEMENT

I would like to thank J. Channusot (Vivone et al., 2014a; Open Remote Sensing, 2015), Shahdoosti and Ghassemian (2014) and Tübitak (Gezgin, 2013) for sharing the datasets that I used.

AUTHOR CONTRIBUTIONS

Methodology and writing-reviewing, T.Ç, and M.C.K; editing, T.Ç; conceptualization and software, M.C.K. All authors have read and legally accepted the final version of the article published in the journal.

CONFLICT OF INTEREST

The authors declare no conflict of interest.

REFERENCES

Aiazzi, B., Alparone, L., Baronti, S., & Garzelli, A. (2002). Context-driven fusion of high spatial and spectral resolution images based on oversampled multiresolution analysis. *IEEE Transactions on geoscience and remote sensing*, *40*(10), 2300-2312. https://doi.org/10.1109/TGRS.2002.803623

Aiazzi, B., Alparone, L., Baronti, S., Garzelli, A., & Selva, M. (2006). MTF-tailored multiscale fusion of high-resolution MS and Pan imagery. *Photogrammetric Engineering & Remote Sensing*, *72*(5), 591-596. https://doi.org/10.14358/PERS.72.5.591

Alparone, L., Aiazzi, B., Baronti, S., Garzelli, A., Nencini, F., & Selva, M. (2008). Multispectral and panchromatic data fusion assessment without reference. *Photogrammetric Engineering & Remote Sensing*, *74*(2), 193-200. https://doi.org/10.14358/PERS.74.2.193

Amro, I., Mateos, J., Vega, M., Molina, R., & Katsaggelos, A. K. (2011). A survey of classical methods and new trends in pansharpening of multispectral images. *EURASIP Journal on Advances in Signal Processing*, *2011*(1), 1-22. https://doi.org/10.1186/1687-6180-2011-79

Ciotola, M., Poggi, G., & Scarpa, G. (2023). Unsupervised Deep Learning-based Pansharpening with Jointly-Enhanced Spectral and Spatial Fidelity. *IEEE Transactions on geoscience and remote sensing*. https://doi.org/10.48550/arXiv.2307.14403

Civicioglu, P., & Besdok, E. (2022). Contrast stretching based pansharpening by using weighted differential evolution algorithm. *Expert Systems with Applications*, *208*, 118144. https://doi.org/10.1016/j.eswa.2022.118144

Civicioglu, P., & Besdok, E. (2024). Pansharpening of remote sensing images using dominant pixels. *Expert Systems with Applications*, *242*, 122783. https://doi.org/10.1016/j.eswa.2023.122783

Civicioglu, P., Besdok, E., Gunen, M. A., & Atasever, U. H. (2020). Weighted differential evolution algorithm for numerical function optimization: a comparative study with cuckoo search, artificial bee colony, adaptive differential evolution, and backtracking search optimization algorithms. *Neural Computing and Applications*, *32*, 3923-3937. https://doi.org/10.1007/s00521-018-3822-5

Feng, Y., Yan, B., Jeon, S., & Yang, X. (2024). A hyperspectral pansharpening method using retrain transformer network for remote sensing images in UAV communications system. *Wireless Networks*, 1-14. https://doi.org/10.1007/s11276-023-03611-2

Garzelli, A. (2014). Pansharpening of multispectral images based on nonlocal parameter optimization. *IEEE Transactions on geoscience and remote sensing*, *53*(4), 2096-2107. https://doi.org/10.1109/TGRS.2014.2354471

Gezgin. (2013). (Accessed:01/11/2023) https://gezgin.gov.tr/geoportal/app/main?execution=e3s1

Ghassemian, H. (2016). A review of remote sensing image fusion methods. *Information Fusion*, *32*, 75-89. https://doi.org/10.1016/j.inffus.2016.03.003

Günen, M. A. (2021). Weighted differential evolution algorithm based pansharpening. *International Journal of Remote Sensing*, *42*(22), 8468-8491. https://doi.org/10.1080/01431161.2021.1976874

Kallel, A. (2014). MTF-adjusted pansharpening approach based on coupled multiresolution decompositions. *IEEE Transactions on geoscience and remote sensing*, *53*(6), 3124-3145. https://doi.org/10.1109/TGRS.2014.2369056

Kurban, T. (2022). Region based multi-spectral fusion method for remote sensing images using differential search algorithm and IHS transform. *Expert Systems with Applications*, *189*, 116135. https://doi.org/10.1016/j.eswa.2021.116135

Lolli, S., Alparone, L., Garzelli, A., & Vivone, G. (2017). Haze correction for contrast-based multispectral pansharpening. *IEEE Geoscience and Remote Sensing Letters*, *14*(12), 2255-2259. https://doi.org/10.1109/LGRS.2017.2761021

Masi, G., Cozzolino, D., Verdoliva, L., & Scarpa, G. (2016). Pansharpening by convolutional neural networks. *Remote Sensing*, *8*(7), 594. https://doi.org/10.3390/rs8070594

Meng, X., Shen, H., Li, H., Zhang, L., & Fu, R. (2019). Review of the pansharpening methods for remote sensing images based on the idea of meta-analysis: Practical discussion and challenges. *Information Fusion*, *46*, 102-113. https://doi.org/10.1016/j.inffus.2018.05.006

Meng, X., Xiong, Y., Shao, F., Shen, H., Sun, W., Yang, G., Yuan, Q., Fu, R., & Zhang, H. (2020). A large-scale benchmark data set for evaluating pansharpening performance: Overview and implementation. *IEEE Geoscience and Remote Sensing Magazine*, *9*(1), 18-52. https://doi.org/10.1109/MGRS.2020.2976696

Open Remote Sensing. (2015). (Accessed:01/11/2023) https://openremotesensing.net/knowledgebase/a-critical-comparison-among-pansharpening-algorithms/

Otazu, X., González-Audícana, M., Fors, O., & Núñez, J. (2005). Introduction of sensor spectral response into image fusion methods. Application to wavelet-based methods. *IEEE Transactions on geoscience and remote sensing*, *43*(10), 2376-2385. https://doi.org/10.1109/TGRS.2005.856106

Palsson, F., Sveinsson, J. R., & Ulfarsson, M. O. (2013). A new pansharpening algorithm based on total variation. *IEEE Geoscience and Remote Sensing Letters*, *11*(1), 318-322. https://doi.org/10.1109/LGRS.2013.2257669

Restaino, R., Vivone, G., Dalla Mura, M., & Chanussot, J. (2016). Fusion of multispectral and panchromatic images based on morphological operators. *IEEE Transactions on Image Processing*, *25*(6), 2882-2895. https://doi.org/10.1109/tip.2016.2556944

Scarpa, G., Vitale, S., & Cozzolino, D. (2018). Target-adaptive CNN-based pansharpening. *IEEE Transactions on geoscience and remote sensing*, *56*(9), 5443-5457. https://doi.org/10.1109/TGRS.2018.2817393

Shahdoosti, H. R., & Ghassemian, H. (2014). Fusion of MS and PAN images preserving spectral quality. *IEEE Geoscience and Remote Sensing Letters*, *12*(3), 611-615. https://doi.org/10.1109/LGRS.2014.2353135

Tu, T., Su, S., Shyn, H., & Huang, P. (2001). A new look at IHS-like image fusion methods. *Information Fusion*. https://doi.org/10.1016/S1566-2535(01)00036-7

Vivone, G. (2019). Robust band-dependent spatial-detail approaches for panchromatic sharpening. *IEEE Transactions on geoscience and remote sensing*, *57*(9), 6421-6433. https://doi.org/10.1109/TGRS.2019.2906073

Vivone, G., Alparone, L., Chanussot, J., Dalla Mura, M., Garzelli, A., Licciardi, G. A., Restaino, R., & Wald, L. (2014a). A critical comparison among pansharpening algorithms. *IEEE Transactions on geoscience and remote sensing*, *53*(5), 2565-2586. https://doi.org/10.1109/TGRS.2014.2361734

Vivone, G., Dalla Mura, M., Garzelli, A., Restaino, R., Scarpa, G., Ulfarsson, M. O., Alparone, L., & Chanussot, J. (2020). A new benchmark based on recent advances in multispectral pansharpening: Revisiting pansharpening with classical and emerging pansharpening methods. *IEEE Geoscience and Remote Sensing Magazine*, *9*(1), 53-81. https://doi.org/10.1109/MGRS.2020.3019315

Vivone, G., Restaino, R., & Chanussot, J. (2017). A regression-based high-pass modulation pansharpening approach. *IEEE Transactions on geoscience and remote sensing*, *56*(2), 984-996. https://doi.org/10.1109/TGRS.2017.2757508

Vivone, G., Restaino, R., & Chanussot, J. (2018). Full scale regression-based injection coefficients for panchromatic sharpening. *IEEE Transactions on Image Processing*, *27*(7), 3418-3431. https://doi.org/10.1109/TIP.2018.2819501

Vivone, G., Restaino, R., Dalla Mura, M., Licciardi, G., & Chanussot, J. (2013). Contrast and error-based fusion schemes for multispectral image pansharpening. *IEEE Geoscience and Remote Sensing Letters*, *11*(5), 930-934. https://doi.org/10.1109/LGRS.2013.2281996

Vivone, G., Simões, M., Dalla Mura, M., Restaino, R., Bioucas-Dias, J. M., Licciardi, G. A., & Chanussot, J. (2014b). Pansharpening based on semiblind deconvolution. *IEEE Transactions on geoscience and remote sensing*, *53*(4), 1997-2010. https://doi.org/10.1109/TGRS.2014.2351754

Wald, L., Ranchin, T., & Mangolini, M. (1997). Fusion of satellite images of different spatial resolutions: Assessing the quality of resulting images. *Photogrammetric engineering and remote sensing*, *63*(6), 691-699.

Yilmaz, C. S., Yilmaz, V., & Gungor, O. (2022). A theoretical and practical survey of image fusion methods for multispectral pansharpening. *Information Fusion*, *79*, 1-43. https://doi.org/10.1016/j.inffus.2021.10.001